

U-WNO: U-Net Enhanced Wavelet Neural Operator for Solving Parametric Partial Differential Equations

Wei-Min Lei^a, Hou-Biao Li^{a,*}

^a*School of Mathematical Sciences, University of Electronic Science and Technology of China, Chengdu, 611731, P. R. China*

Abstract

High-frequency features are critical in multiscale phenomena such as turbulent flows and phase transitions, since they encode essential physical information. The recently proposed Wavelet Neural Operator (WNO) utilizes wavelets' time-frequency localization to capture spatial manifolds effectively. While its factorization strategy improves noise robustness, it suffers from high-frequency information loss caused by finite-scale wavelet decomposition. In this study, a new U-WNO network architecture is proposed. It incorporates the U-Net path and residual shortcut into the wavelet layer to enhance the extraction of high-frequency features and improve the learning of spatial manifolds. Furthermore, we introduce an adaptive activation mechanism to mitigate spectral bias through trainable slope parameters. Extensive benchmarks across seven PDE families (Burgers, Darcy flow, Navier-Stokes, etc.) show that U-WNO achieves 45–83% error reduction compared to baseline WNO, with mean L_2 relative errors ranging from 0.043% to 1.56%. This architecture establishes a framework combining multiresolution analysis with deep feature learning, addressing the spectral-spatial tradeoff in operator learning. Code and data used are available on <https://github.com/WeiminLei/U-WNO>. `git`.

Keywords: Partial Differential Equations; Deep learning; Wavelet Neural Operator; Operator Learning

1. Introduction

In recent years, Neural Networks (NN) [1] have been widely used in computational science to solve classical applied mathematics problems. This is due to their strong approximation capabilities and ability to handle nonlinear systems. Natural systems are governed by conservation and constitutive laws. Modeling complex constitutive laws using PDEs is a popular approach in various fields of science and engineering disciplines [2–4]. In most cases, the preferred methods for solving these PDEs, due to the lack of analytical solutions, are the Finite Element Method (FEM) [5], isogeometric analysis [6], the Finite Difference Method (FDM) [7], and the Finite Volume Method (FVM) [8]. Sometimes, in science and engineering, it becomes

*Corresponding author

Email address: lihoubiao0189@163.com (Hou-Biao Li)

necessary to solve PDEs with different parameters, such as domain geometries, source functions, and initial or boundary conditions (ICs and BCs). These types of PDEs are often referred to as parametric PDEs. However, the computational cost of the traditional numerical schemes described above is high in such cases, as they require independent calculations for each combination of input parameters. In recent years, several approaches using Machine Learning (ML) [9] have been proposed as faster alternatives to numerical simulations [10]. For example, Physics-Informed Neural Networks (PINNs) [11], Deep Galerkin methods (DGM) [12], and Deep Ritz method (DRM) [13] satisfy given governing equations and boundary conditions by constraining the output of NN. However, when solving parametric PDEs using these methods, it is impractical to train a model individually for each PDE parameter. Therefore, deep learning methods for solving parametric PDEs are often considered.

Deep learning (DL) methods for solving parametric partial differential equations are usually divided into two categories:

(1) By combining meta-learning [14] etc., the aforementioned schemes are used to solve parametric PDEs. For example, some researchers have proposed using transfer learning [15] or meta-learning to fine-tune these schemes on the original trained network for rapid generalization to new parameters. Ref. [13] recommends a transfer learning approach that utilizes a model trained for one task as the initial model for training another task, which can accelerate the training of PINNs. This method is effective in the case of small parameter variation ranges, but not in the case of large parameter variation ranges. Therefore, based on the minimum energy path theory, the PDE parameters are set as the trainable parameters of the NN, and the low-loss path is "preset" to ensure training stability and guide the migration of the remaining network weights [16]. Based on the idea of Meta-Learning, a Meta-Learning PINN (Meta-PINN) [17] is designed for plasma simulation acceleration. Some researchers have combined the Reptile algorithm [18] with PINNs to accelerate the solution of parametric PDEs [19]. Meta-MgNet [20] is a work that treats solving parametric PDEs as a Meta-Learning problem. Meta-MgNet leverages the similarity between tasks to adaptively generate a good smoothing operator, which speeds up the solution process. Inspired by the Reduced Basis Method (RBM) [21], Dr. Yanlai Chen designed a pre-trained PINN (GPT-PINN) for parametric PDEs [22].

(2) Another approach utilizes a neural network (NN) to learn how to map the parameters of partial differential equations (PDEs) to their solutions. For example, the Deep Operator Network (DeepONet) [23] introduces two nonlinear operator theories that can be implemented using an NN architecture. DeepONet uses a trunk net and a branch net to encode the parameters and spatial positions of the PDEs, respectively. It combines the outputs of these two networks to obtain the solution of the PDEs. In addition, the Fourier Neural Operator (FNO) [24] directly parameterizes the integral kernel in the Fourier space, resulting in an NN architecture with stronger representation capabilities. By approximating the Green function using the powerful fitting ability of the NN, it transforms the integration over the entire control domain of the PDEs into the integration over the node domain. Recently, a graph neural operator (GNO) for parametric

PDEs is proposed [25]. To reduce the complexity of the calculation, the Multipolar Graph Neural Operator (MGNO) [26] is introduced, which reduces the approximation cost of the kernel function. However, FNO suffers from a lack of spatial resolution due to the frequency localization of the FFT basis function [27], leading to underperformance in PDEs with complex geometries. To address this limitation, the Wavelet Neural Operator (WNO) [28, 29] is proposed, which uses the wavelet transform [30] to learn the spatial frequency positioning and mode changes in the input. WNO can be seen as a more general case of the previously proposed FNO. While WNO excels at learning complex nonlinear differential operators regardless of geometric structure, it restricts the parameterization of neural network weights to high-level wavelet decomposition. This helps mitigate the effects of data noise but hinders the extraction of high-frequency features, leading to decreased accuracy. To address this issue, we propose an enhanced version of WNO called U-WNO:

- Firstly, the U-Net [31] path is incorporated into the wavelet layer of the WNO, which samples the data at various scales. This enables U-WNO to reconstruct information at different frequency scales. Based on the U-Net path, the U-WNO can extract and fuse potential features more effectively.
- By introducing residual shortcuts into the wavelet layer, we ensure hierarchical propagation of complete input function information across scales. This enhances the performance of neural operators in spatial domains.
- Finally, because of the Spectral Bias [32] of the NN, we apply the Adaptive Activation Function [33–35] to improve the convergence speed and accuracy of the network.

The structure of this article is as follows. In Section 2, we introduced the general content of neural operators. We describe our proposed methodology in detail in Section 3. In Section 4, we conduct numerical simulations to demonstrate the effectiveness of our method. Finally, We conclude with some thoughts on possible directions for further research in Section 5.

2. Problem setting and neural operators

An operator is a mapping between an infinitely dimensional input and output function space. Let $D \in \mathbb{R}^d$ be the d-dimensional domain of the boundary ∂D . For the fixed domains $D = (a, b)$ and $x \in D$, consider a PDE that maps the input function space, i.e., the space containing the source term $f(x, t) : D \mapsto \mathbb{R}$, the initial condition $u(x, 0) : D \mapsto \mathbb{R}$, and the boundary condition $u(\partial D, t) : D \mapsto \mathbb{R}$ to the solution space $u(x, t) : D \mapsto \mathbb{R}$, where t is the time coordinate. We aim to learn an operator from the input function to the solution space $u(x, t)$. Now, we define two complete norm vector spaces $(\mathcal{A}, \|\cdot\|_{\mathcal{A}})$ and $(\mathcal{U}, \|\cdot\|_{\mathcal{U}})$ that take the values of a given partial derivative number in \mathbb{R}^{d_a} and \mathbb{R}^{d_u} . These function spaces, often referred to as Banach spaces, are represented as $\mathcal{A} := \mathcal{C}(D; \mathbb{R}^{d_w})$ and $\mathcal{U} := \mathcal{C}(D; \mathbb{R}^{d_w})$. For the given domains $D \in \mathbb{R}^d$ and

the canonical spaces $(\mathcal{A}, \|\cdot\|_{\mathcal{A}})$ and $(\mathcal{U}, \|\cdot\|_{\mathcal{U}})$, our goal is to learn the nonlinear operators $\mathcal{D} : \mathcal{A} \mapsto \mathcal{U}$. Once successful, a series of PDE solutions can be obtained for different input parameter sets $a \in \mathcal{A}$. If there exists a differential operator \mathcal{N} that maps the function spaces to null space, i.e., $\mathcal{N} : \mathcal{A} \times \mathcal{U} \mapsto \mathcal{O}$, where \mathcal{O} is the null space, then the parametric PDEs take the form:

$$\mathcal{N}(a, u) = 0, \quad \text{in } D \subset \mathbb{R}^d. \quad (2.1)$$

The PDE is defined on a d -dimensional bounded domain, $D \in \mathbb{R}^d$, with the boundary ∂D , where the boundary condition is expressed as:

$$u = g, \quad \text{in } \partial D. \quad (2.2)$$

The input and output functions in the function spaces \mathcal{A} and \mathcal{U} are represented by $a : D \mapsto a(x \in D) \in \mathbb{R}^{d_a}$ and $u : D \mapsto u(x \in D) \in \mathbb{R}^{d_u}$. Considering $u_j = \mathcal{D}(a_j)$, we have access to N pairs of $\{(a_j, u_j)\}_{j=1}^N$. Then, our goal is to approximate \mathcal{D} by a neural network (NN) as

$$\mathcal{D} : \mathcal{A} \times \boldsymbol{\theta}_{NN} \mapsto \mathcal{U}, \quad \boldsymbol{\theta}_{NN} = \{\mathcal{W}_{NN}, \mathbf{b}_{NN}\}, \quad (2.3)$$

where $\boldsymbol{\theta}_{NN}$ denotes the finite-dimensional parameter domain of the NN. Although the input and output functions a_j and u_j are continuous, for numerical execution, we discretize the field D with n_D points $\{x_p\}_{p=1}^{n_D}$. Thus, for N sets of input and output pairs, supposing we have access to the dataset $\{a_j \in \mathbb{R}^{n_D \times d_a}, u_j \in \mathbb{R}^{n_D \times d_u}\}_{j=1}^N$. The goal is to develop a network capable of utilizing data to learn the operator \mathcal{D} . For featuring a multidimensional kernel convolution, the input $a(x) \in \mathcal{A}$ is lifted to a higher-dimensional space through the local transformation $P(a(x)) : \mathbb{R}^{d_a} \mapsto \mathbb{R}^{d_v}$ and represent the higher-dimensional space as $v_0(x) = P(a(x))$, where $v_0(x)$ takes the value in \mathbb{R}^{d_v} . In addition, L steps are required to converge. We apply L iterations $v_{i+1} = G(v_i)$ for $i = 0, \dots, L$ on $v_0(x)$, where the function $G : \mathbb{R}^{d_v} \mapsto \mathbb{R}^{d_v}$ takes its value in \mathbb{R}^{d_v} . Once the iteration is done, we define another local transformation $Q(v_L(x)) : \mathbb{R}^{d_v} \mapsto \mathbb{R}^{d_u}$ and convert the output $v_L(x)$ back to the solution space $u(x) = Q(v_L(x))$. $v_{j+1} = G(v_j)$ is defined as

$$v_{j+1}(x) := \sigma((K(a; \phi) * v_j)(x) + Wv_j(x)), \quad x \in D, \quad j \in [0, L], \quad (2.4)$$

where $\sigma(\cdot) : \mathbb{R} \rightarrow \mathbb{R}$ is a nonlinear activation function, $W : \mathbb{R}^{d_v} \rightarrow \mathbb{R}^{d_v}$ is a linear transformation, and $K : \mathcal{A} \times \boldsymbol{\theta} \rightarrow \mathcal{L}(\mathcal{U}, \mathcal{U})$ is an integral operator on $\mathcal{C}(D; \mathbb{R}^{d_v})$. In the NN setup, we set $K(a; \phi)$ to represent a kernel integral operator parameterized by $\phi \in \boldsymbol{\theta}$. The kernel integral operator $K(a; \phi)$ is defined as,

$$(K(a; \phi) * v_j)(x) := \int_{D \in \mathbb{R}^d} k(a(x), x, y; \phi) v_j(y) dy; \quad x \in D, \quad j \in [0, L], \quad (2.5)$$

where $k_\phi : \mathbb{R}^{2d+d_a} \mapsto \mathbb{R}^{d_v \times d_v}$ is an NN parameterized by $\phi \in \boldsymbol{\theta}$. Suppose some kernel $k \in \mathcal{C}(D; \mathbb{R}^{d_v})$ then we learn κ_ϕ from the data with the concept of degenerate kernels, so that,

$$\|(k_\phi(a) - k(a))v\| \leq \|k_\phi(a) - k(a)\| \|v\|, \quad (2.6)$$

and $k_\phi \rightarrow k$. Since the kernel $k \in \mathcal{C}(D)$ and $K \in \mathcal{L}(\mathcal{C}(D; \mathbb{R}^{d_v}))$ together define the infinite-dimensional space, Eq.(2.4) can learn the mapping of any infinite-dimensional function space. When it comes to approximating nonlinear operators, the structure of Eq.(2.4) follows that of a traditional neural network. To train the network, we define an appropriate loss function, $\mathcal{L} = \mathcal{U} \times \mathcal{U}$ as follows:

$$\theta_{NN} = \arg \min_{\theta_{NN}} \mathcal{L}(\mathcal{D}(a), \mathcal{D}(a, \theta)). \quad (2.7)$$

Then, the Eq. (2.7) is minimized in a data-driven way to obtain the best parameters of the network. Finally, we obtain the neural operator.

3. Proposed Methodology

3.1. Wavelet Neural Operator [28]

To delete the term $a(x, y)$ from Eq. (2.5), change the kernel to $k_\phi(x - y)$. We rewrite Eq.(2.5) as follows:

$$(K(\phi) * v_j)(x) := \int_{D \in \mathbb{R}^d} k(x - y; \phi) v_j(y) dy, \quad x \in D, \quad j \in [0, L]. \quad (3.1)$$

This is consistent with the convolution operator. The kernel k_ϕ is learned by parameterization in the wavelet domain. The continuous wavelet transform (CWT) is computationally expensive, so the discrete wavelet transform (DWT) is chosen by learning the kernel in the wavelet domain. The above convolution is then performed on the wavelet decomposition coefficients. Let $\psi(x) \in \mathcal{L}^2(\mathbb{R})$ be an orthogonal parent wavelet. Assuming that $\mathcal{W}(\Gamma)$ and $\mathcal{W}^{-1}(\Gamma_w)$ are the forward and reverse discrete wavelet transforms of any function $\Gamma : D \mapsto \mathbb{R}^{d_v}$, the forward and reverse wavelet transforms of the function Γ with scaling and shift parameters $m \in \mathbb{R}^+$ and $\tau \in \mathbb{R}$ are given by the following integral pairs,

$$\begin{aligned} (\mathcal{W}\Gamma)_j(m, \tau) &= \frac{1}{\sqrt{2^m}} \int_D \Gamma(x) \psi\left(\frac{x - \tau 2^m}{2^m}\right) dx, \\ (\mathcal{W}^{-1}\Gamma_w)_j(x) &= \frac{1}{C_\psi \sqrt{2^m}} \int_0^\infty \int_D (\Gamma_w)_j(m, \tau) \tilde{\psi}\left(\frac{x - \tau 2^m}{2^m}\right) d\tau \frac{dm}{m^2}, \end{aligned} \quad (3.2)$$

The term C_ψ is called the allowable constant and has the range $0 < C_\psi < \infty$. The expression of C_ψ is

$$C_\psi = 2\pi \int_D \frac{|\psi(\omega)|^2}{|\omega|} d\omega. \quad (3.3)$$

Applying the convolution theorem, let $R_\phi = \mathcal{W}(k_\phi)$, Eq.(3.1) on the wavelet domain is expressed as

$$(\mathcal{K}(\phi) * v_j)(x) = \mathcal{W}^{-1}(R_\phi \cdot \mathcal{W}(v_j))(x), \quad x \in D. \quad (3.4)$$

R_ϕ is parameterized only at the highest decomposition level, so we have $\mathcal{W}(v_t) \in \mathbb{R}^{n/2^m \times d_v}$ in the m-level of DWT. The length of the wavelet coefficient is also affected by the number of vanishing moments of the orthogonal parent wavelet. Therefore, it is more appropriate to write $\mathcal{W}(v_t, m) \in \mathbb{R}^{\zeta \times d_v}$, where the ζ wavelet coefficient supports the length of the width. Thus, direct parameterization of R_ϕ in the wavelet space is

performed by integrating the parameter ϕ into the convolution of the value tensor of $(\zeta \times d_v \times d_v)$. To rewrite Eq.(3.4), we can write the convolution of the weight tensor $R \in \mathbb{R}^{\zeta \times d_v \times d_v}$ and $\mathcal{W}(v_t, m) \in \mathbb{R}^{\zeta \times d_v}$ as,

$$(R \cdot \mathcal{W}(v_j, m))_{I_1, I_2}(x) = \sum_{I_3=1}^{d_v} R_{I_1, I_2, I_3} \mathcal{W}(v_j, m)_{I_1, I_3}, \quad I_1 \in [1, \zeta], \quad I_2, I_3 \in d_v. \quad (3.5)$$

The WNO architecture consists of three steps:

- The input function $a(x)$ is elevated to a high-dimensional space $v_0(x) = P(a(x))$ by transforming P with a fully connected NN (FNN).
- Application of wavelet layer: $v_0 \mapsto v_1 \mapsto \dots \mapsto v_L$, where v_j for $j = 0, 1, \dots, L$ is a sequence of functions taking the value of the channel dimension c in \mathbb{R}^c .
- Use the FNN transform Q to project v_L back to the original space $u(x) = Q(v_L(x))$.

In each of the wavelet layers, there are

$$v_{j+1}(x) := \sigma \left((\mathcal{K}v_j)(x) + W(v_j(x)) \right), \forall x \in D, \quad (3.6)$$

where \mathcal{K} is the kernel integral transform defined above and W is a linear operator, both of which are learnable. σ is an activation function that introduces nonlinearities to each wavelet layer.

3.2. The Spectral Bias and Adaptive Activation Function

We first review the use of Neural Tangent Kernel (NTK) [36] theory to study the Spectral Bias of NN [37] and verify it empirically. Then the experiment confirms that the Spectral Bias of NN can be overcome by introducing the Adaptive Activation Function. Let $f(x, \boldsymbol{\theta})$ be a fully connected neural network (FNN) with weight $\boldsymbol{\theta}$ initialized by the Gaussian distribution $\mathcal{N}(0, 1)$. Given a dataset $\{\mathbf{X}_{\text{train}}, \mathbf{Y}_{\text{train}}\}$, where $\mathbf{X}_{\text{train}} = (x_i)_{i=1}^N$ is the input and $\mathbf{Y}_{\text{train}} = (y_i)_{i=1}^N$ is the output, we consider the mean square loss $\mathcal{L}(\boldsymbol{\theta}) = \frac{1}{N} \sum_{i=1}^N |f(x_i, \boldsymbol{\theta}) - y_i|^2$ using a very small learning rate η . The neural tangent kernel operator \mathbf{K} can be defined as follows:

$$K_{ij} = K(x_i, x_j) = \left\langle \frac{\partial f(x_i, \boldsymbol{\theta})}{\partial \boldsymbol{\theta}}, \frac{\partial f(x_j, \boldsymbol{\theta})}{\partial \boldsymbol{\theta}} \right\rangle. \quad (3.7)$$

The NTK theory states that during gradient descent dynamics with infinitesimal learning rates, the kernel K converges to a deterministic kernel K^* and remains unchanged during training as the width of the network approaches infinity. Additionally, we have

$$\frac{df(\mathbf{X}_{\text{train}}, \boldsymbol{\theta}(t))}{dt} \approx -\mathbf{K} \cdot (f(\mathbf{X}_{\text{train}}, \boldsymbol{\theta}(t)) - \mathbf{Y}_{\text{train}}), \quad (3.8)$$

$\boldsymbol{\theta}(t)$ denotes the parameters of the network in the iteration t , $f(\mathbf{X}_{\text{train}}, \boldsymbol{\theta}(t)) = (f(x_i, \boldsymbol{\theta}(t)))_{i=1}^N$. Then, it has the following form

$$f(\mathbf{X}_{\text{train}}, \boldsymbol{\theta}(t)) \approx (I - e^{-\mathbf{K}t}) \cdot \mathbf{Y}_{\text{train}}. \quad (3.9)$$

Since the kernel \mathbf{K} is positive semidefinite, let its spectral decomposition $\mathbf{K} = \mathbf{Q}^T \mathbf{\Lambda} \mathbf{Q}$, and since $e^{-\mathbf{K}t} = \mathbf{Q}^T e^{-\mathbf{\Lambda}t} \mathbf{Q}$, we have

$$\mathbf{Q}(f(\mathbf{X}_{\text{train}}, \boldsymbol{\theta}(t)) - \mathbf{Y}_{\text{train}}) = -e^{-\mathbf{\Lambda}t} \mathbf{Q} \mathbf{Y}_{\text{train}}. \quad (3.10)$$

This means that components of an objective function corresponding to a kernel eigenvector with larger eigenvalues will learn more quickly. For traditional FNN, the eigenvalue of NTK decays rapidly. As a result, convergence to the high-frequency components of the objective function is very slow. Next, we use FNN to approximate the following function, and the results are shown in Figure 1. On the left, we can observe that even after 15,000 epochs, the network poorly fits the function with high-frequency components. From the figure on the right, we can see that the network first fits the low-frequency components of $f(x)$ and then gradually starts to fit the high-frequency components of $f(x)$.

$$f(x) = \sin(2x) + \sin(7x) + \sin(16x). \quad (3.11)$$

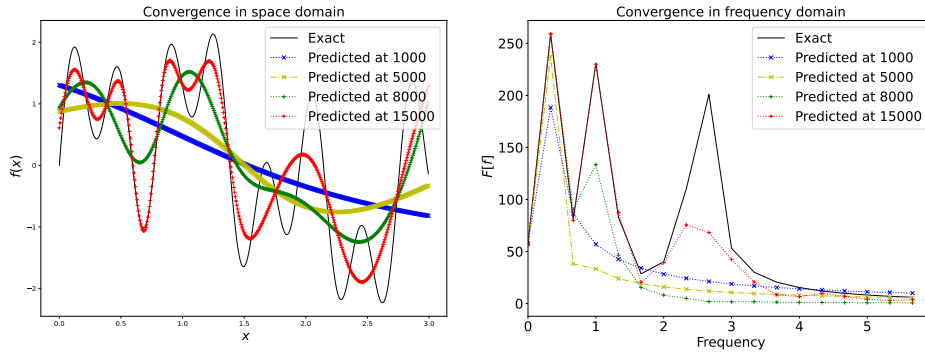


Figure 1 The convergence of FNN in the spatial domain (left) and frequency domain (right) when approaching $f(x)$.

The form of the Adaptive Activation Function[33–35] is as follows, and it has been utilized in PINNs to enhance the network’s convergence speed. We employ an FNN with an Adaptive Activation Function to fit $f(x)$ under identical conditions, and the experimental results are depicted in Figure 2. Based on this figure, we can infer that the Adaptive Activation Function expedites the learning process of the high-frequency components of $f(x)$ and mitigates the network’s spectral bias

$$\sigma(nax), \quad (3.12)$$

where a is a trainable adaptive parameter, such an activation function is more likely to generate high-frequency nonlinear parts. This speeds up the network’s learning of high-frequency information of the data.

$n \geq 1$ is the scaling factor selected by experience. For the hyper-parameter n , empirical studies showed $n = 10$ optimally balances convergence speed and stability across our test cases, though adaptive tuning strategies may further improve performance.

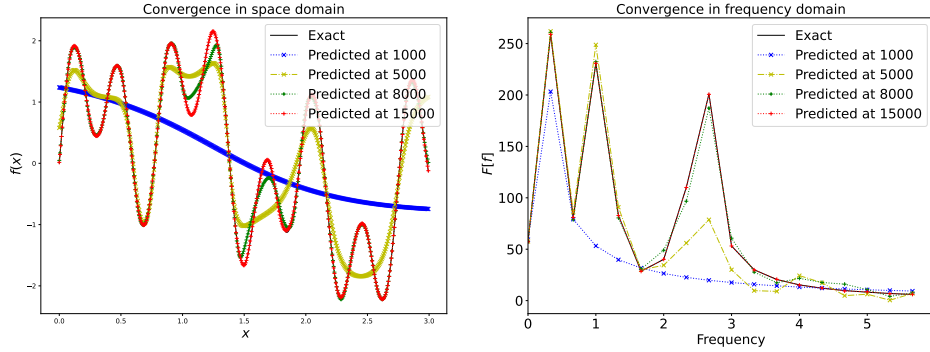


Figure 2 The convergence of FNN with Adaptive Activation Function in the spatial domain (left) and frequency domain (right) when approaching $f(x)$.

3.3. Proposed methods

As we previously discussed, WNO chooses to parameterize R_ϕ at the highest scale of the DWT. It retains only the information from the highest scale wavelet coefficients, allowing for a finite-dimensional parameterized space. This approach enables accurate data analysis and efficient learning. With the help of the wavelet transform’s characteristics, WNO can effectively learn highly nonlinear differential operators, regardless of the geometry. However, WNO is not enough to extract high-frequency information from the data.

The U-Net is capable of handling local convolution, and it directly transmits feature maps from the encoder to the decoder, aiding in the preservation of more detailed information. Our introduction of the U-Net framework aims to improve WNO’s ability to reconstruct high-frequency data. The U-Net structure is depicted in Figure 3, where it subsamples data to various scales. This allows for obtaining high-frequency information through convolution operations at different scales, thereby enhancing the expressiveness of neural operators on high-dimensional information. At the same time, we also introduce residual shortcuts to ensure that each modified wavelet layer can enhance the performance of neural operators in the spatial domain. We use the Adaptive Activation Function described in Section 3.2. Thus, in the U-WNO layer, Eq.(3.6) is rewritten as

$$\begin{aligned}
 v_{j+1}(x) &:= \sigma(na(\mathcal{K}v_j)(x) + W(v_j(x))), & j = 0 \\
 v_{j+1}(x) &:= \sigma(na(\mathcal{K}(v_j + v_0))(x) + W(v_j(x)) + \mathcal{U}(v_j(x))), & j = 1, 2, \dots, L
 \end{aligned}
 , \forall x \in D. \quad (3.13)$$

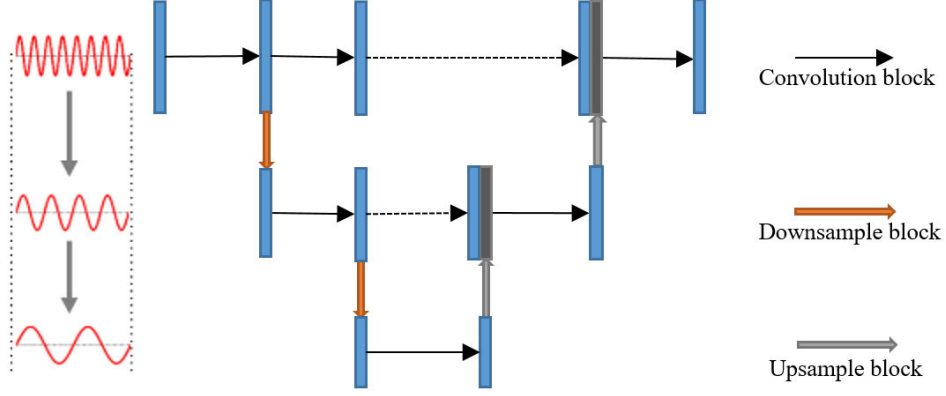


Figure 3 The architecture of U-Net path added to the U-WNO model.

Where \mathcal{K} , W are the same as in WNO. σ is an activation function. \mathcal{U} is the U-Net convolutional neural network operator. The size of the convolution kernel used in the U-Net path is different from that in W , which helps to improve the ability of the network to extract features.

The U-WNO architecture also consists of three steps. First, as with WNO, the input function $a(x)$ is transformed to the higher-dimensional space $v_0(x) = P(a(x))$, and then the U-WNO layer is applied: $v_0 \mapsto v_1 \mapsto \dots \mapsto v_L$, where v_j for $j = 0, 1, \dots, L$. Finally, v_L is projected back to the original space using Q , resulting in $u(x) = Q(v_L(x))$. Figure 4 provides a schematic of the U-WNO architecture. The step-by-step implementation of U-WNO is provided in Algorithm 1.

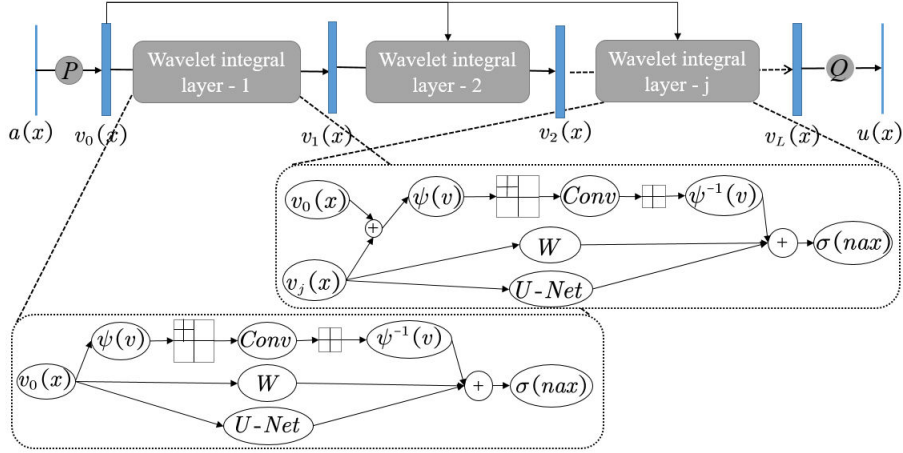


Figure 4 U-WNO model architecture. $a(x)$ is the input function, P and Q are FNNs, and $u(x)$ is the output function. In the U-WNO layer, we use the Wavelet transform denoted as ψ and R as a parameterization in Wavelet space. The inverse Wavelet transform is denoted as ψ^{-1} , and the linear bias term is referred to as W . The activation function is represented by σ . In the U-WNO layer, we utilize the residual shortcut to obtain complete information from v_0 . Additionally, we add the U-Net path to enhance the performance of U-WNO in capturing high-frequency information.

Algorithm 1 Algorithm of the U-WNO

Requirements: N -samples of the pair $\{a(x) \in \mathbb{R}^{n_D \times d_a}, u(x) \in \mathbb{R}^{n_D \times d_u}\}$, coordinates $x \in D$, and network hyperparameters.

- 1: Stack the inputs: $\{a(x), x\} \in \mathbb{R}^{n_D \times 2d_a}$.
- 2: **for** epoch = 1, ..., epochs **do**
- 3: Uplift the input using transformation $P(\cdot) : v_0(x) \in \mathbb{R}^{n_D \times d_v} = P(\{a(x), x\} \in \mathbb{R}^{n_D \times 2d_a})$.
- 4: **for** $j = 0, \dots, L$ perform the iterations: $v_{j+1} = G(v_j)$ **do**
- 5: **if** $j = 0$ **then**
- 6: Decompose the input using wavelet decomposition: $\mathcal{W}(v_j(x)) \in \mathbb{R}^{n_D/2^m \times d_v}$.
- 7: Parameterize the kernel k_ϕ in the wavelet space : $R_\phi * \mathcal{W}(v_j(x))$, see Eq.(3.5)
- 8: Reconstruct the convoluted input: $v_{j+1}^1(x) = \mathcal{W}^{-1}(R_\phi * \mathcal{W}(v_j(x)))$, see Eq.(3.4)
- 9: Perform the linear transform: $v_{j+1}^2(x) = W * v_j(x)$ using Convolutional Neural Networks.
- 10: Computes the output of the U-Net: $v_{j+1}^3(x) = \mathcal{U}(v_j(x))$.
- 11: Add the outputs of step 8, 9 and 10: $\tilde{v}_{j+1}(x) \in \mathbb{R}^{n_D \times d_v} = (v_{j+1}^1 + v_{j+1}^2 + v_{j+1}^3)(x)$, see Eq.(3.13)
- 12: **else**
- 13: Introduce residual shortcuts and proceed to Steps 6, 7, and 8: $\mathcal{W}(v_j(x) + v_0(x)) \in \mathbb{R}^{n_D/2^m \times d_v}$.
- 14: Proceed to Step 7 and 8: $v_{j+1}^1(x) = \mathcal{W}^{-1}(R_\phi * \mathcal{W}(v_j(x) + v_0(x)))$.
- 15: Proceed to Step 9 and 10: $v_{j+1}^2(x) = W * v_j(x)$, $v_{j+1}^3(x) = \mathcal{U}(v_j(x))$.
- 16: Add the outputs of step 14 and 15: $\tilde{v}_{j+1}(x) \in \mathbb{R}^{n_D \times d_v} = (v_{j+1}^1 + v_{j+1}^2 + v_{j+1}^3)(x)$.
- 17: **if** $j \neq L$ **then**
- 18: Apply the activation to complete the iteration: $v_{j+1} \in \mathbb{R}^{n_D \times d_v} = \sigma(na\tilde{v}_{j+1}(x))$.
- 19: **end if**
- 20: **end if**
- 21: **end for**
- 22: Apply an activated lifting transformation: $r(x) \in \mathbb{R}^{n_D \times d_r} = \sigma(Q_1(v_L(x)))(Q_1(\cdot) : \mathbb{R}^{d_v} \mapsto \mathbb{R}^{d_r}$ is a (FNN).
- 23: Compute the final output: $\hat{u}(x) \in \mathbb{R}^{n_D \times d_u} = Q_2(r(x))(Q_2(\cdot) : \mathbb{R}^{d_r} \mapsto \mathbb{R}^{d_u}$ is a FNN).
- 24: Compute the loss: $\mathcal{L}(u, \hat{u})$.
- 25: Compute the gradient of the loss: $\frac{\partial \mathcal{L}(u, \hat{u})}{\partial \theta_{NN}}$.
- 26: Update the parameters of the network using the gradient.
- 27: **end for**

Output: Prediction of the solution of the PDEs

4. Numerical experiments

In this section, the proposed U-WNO is applied to parametric PDEs, which include various problems in fluid dynamics, gas dynamics, traffic flow, atmospheric science, and phase field modeling.

We compare the results obtained by four popular neural operators and their variants: (a) DeepONet, (b) FNO, (c) Multiwavelet transform operator (MWT) [38], (d) WNO. The U-WNO architecture consists of four U-WNO layers, each of which is activated by the GELU or MISH activation function. The mother wavelet is taken from the Daubechies family [39]. The dataset size, wavelet, wavelet tree level for all cases and the number of layers in the network against each equation are provided in Table 1. For training the U-WNO, we use the Adam optimizer with an initial learning rate of 0.001. During optimization, the learning rate decays at a rate of 0.5 every 50 epochs. The number of epochs used to train the U-WNO architecture is shown in Table 2. The batch size in the data loader is 20. Numerical experiments are performed on two NVIDIA Tesla V100-PCIE-32GB GPUs. In all experiments in this paper, the former part of the dataset is selected for the training set, and the latter part of the dataset is selected for the test set, which is consistent with the benchmark methods such as FNO and WNO. The results of solving PDEs with different parameters are summarized in Table 3. The results show that the mean L_2 relative test error of the proposed U-WNO ranges from 0.043% to 1.56%, and U-WNO produces the lowest error in seven out of nine cases. In the remaining two problems, U-WNO is not the most accurate, but it is not far from the best result. Compared to WNO, U-WNO demonstrates significantly improved accuracy in all nine cases. Table 4 shows the number of parameters and the time per epoch for WNO and U-WNO. Although the number of parameters of U-WNO is increased by about 75% on average compared with WNO, the average increase of the training time of a single epoch of U-WNO is less than 40%, and the final accuracy is significantly improved, which indicates that the increase in computational cost is acceptable. The loss function used in U-WNO training and testing is the L_2 relative error function:

$$Loss = \frac{1}{N} \sum_{i=1}^N \frac{\|u - \hat{u}\|_2}{\|u\|_2} \quad (4.1)$$

where N is the number of samples. \hat{u} is the predicted value obtained by U-WNO inference, u is the true value of the sample.

4.1. 1D Burgers equation

For the first example, we choose the Burgers equation with different initial conditions. The 1D Burgers equation is frequently employed to mathematically represent fluid dynamics and gas dynamics, traffic flow, and other braided formations. The 1D Burgers equation with periodic boundary conditions can be expressed mathematically as follows:

Table 1 The relevant parameter information of the U-WNO.

Examples	Number of samples		Wavelet	m	Network dimensions		$\sigma(\cdot)$	
	Training	Testing			FNN1	FNN2		
Burgers	time-independent	1000	100	db6	8	64	128	MISH
	time-dependent	480	20	db6	6	40	128	MISH
Advection	time-independent	900	100	db6	3	96	128	MISH
	time-dependent	1000	100	db6	3	80	128	MISH
Darcy	rectangular	1000	100	db4	4	64	128	GELU
	triangular	1000	100	db6	3	64	128	MISH
Allen-Cahn		1000	100	db6	2	64	128	MISH
Non-homogeneous Poisson		1000	100	db4	4	64	128	GELU
Navier-Stokes		1000	100	db4	3	26	128	GELU

Table 2 The number of training epochs for different network structures and examples.

Examples	Network architecture					
	DeepONet	FNO	MWT	WNO	U-WNO	
Burgers	time-independent	500000	500	500	500	500
	time-dependent	-	-	-	500	500
Advection	time-independent	-	-	-	500	500
	time-dependent	250000	500	500	500	500
Darcy	rectangular	100000	500	500	500	500
	triangular	20000	500	500	500	500
Allen-Cahn		100000	500	500	500	500
Non-homogeneous Poisson		-	500	-	500	500
Navier-Stokes		100000	500	500	500	500

$$\begin{aligned}
\partial_t u(x, t) + \frac{1}{2} \partial_x u^2(x, t) &= \nu \partial_{xx} u(x, t), \quad x \in (0, 1), t \in (0, 1] \\
u(x = 0, t) &= u(x = 1, t), \quad x \in (0, 1), t \in (0, 1] \\
u(x, 0) &= u_0(x), \quad x \in (0, 1).
\end{aligned} \tag{4.2}$$

Where $\nu \in \mathbb{R}_+$ is the viscosity of the flow and $u_0 \in L^2_{\text{ner}}((0, 1); \mathbb{R})$ is the initial condition. The initial conditions $u_0(x)$ are generated using a Gaussian random field: $\mu = \mathcal{N}(0, 625(-\Delta + 25I)^{-2})$. Consider periodic boundary conditions of the form $u(x - \pi, t) = u(x + \pi, t); x \in (0, 1), t \in (0, 1]$. The aim here is

Table 3 Mean L_2 relative error between the exact and predicted results.

Examples		Network architecture					
		DeepONet	FNO	dgFNO+ ^a	MWT	WNO	U-WNO
Burgers	time-independent	2.15%	1.60%	-	0.19%	1.87%	1.56%
	time-dependent	-	-	-	-	0.23%	0.043%
Advection	time-independent	-	-	-	-	0.85%	0.053%
	time-dependent	0.32%	47.7%	0.62%	10.22%	0.62%	0.059%
Darcy	rectangular	2.98%	1.08%	-	0.89%	1.84%	0.62%
	triangular	2.64%	-	7.82%	0.87%	0.77%	0.20%
Allen-Cahn		17.7%	0.93%	-	4.84%	0.22%	0.095%
Non-homogeneous Poisson		-	0.16%	-	-	0.36%	0.044%
Navier-Stokes		1.78%	1.28%	-	0.63%	3.16%	0.96%

^a Note that in complex geometric conditions, FNO does not work, thus we use dgFNO+[40].

Table 4 The number of parameters for different network structures and the time required for each epoch.

Examples		WNO		U-WNO	
		Parameters	Time	Parameters	Time
Burgers	time-independent	484033	6.32s	1159362	7.30s
	time-dependent	243217	32.97s	506258	44.29s
Advection	time-independent	1082273	3.73s	2599074	5.03s
	time-dependent	756497	63.68s	1807378	96.71s
Darcy	rectangular	7955201	6.74s	10596866	9.54s
	triangular	16802561	11.20s	18738434	16.63s
Allen-Cahn		16802561	6.24s	19261442	10.04s
Non-homogeneous Poisson		14770945	25.51s	17412610	39.33s
Navier-Stokes		1448207	33.72s	2562532	42.70s

to learn the operator $\mathcal{D} : u_0(x) \mapsto u(x, 1)$. We choose $\nu = 0.1$ and a spatial resolution of 1024 for the experiments. The dataset is taken from Ref. [24].

Results: The prediction results and the mean test L_2 relative error are provided in Figure 5 and Table 3. From Table 3, the MWT obtains the lowest error, followed by the proposed U-WNO. The error of U-WNO is lower than DeepONet and FNO, and U-WNO significantly reduces the error compared with WNO. Although the error predicted using U-WNO is higher than that of the MWT from a quantitative point of view, Figure 5 shows that the difference between the predicted solutions and true solutions is small. This

shows that although U-WNO is not the best, it still has good expressiveness in this problem.

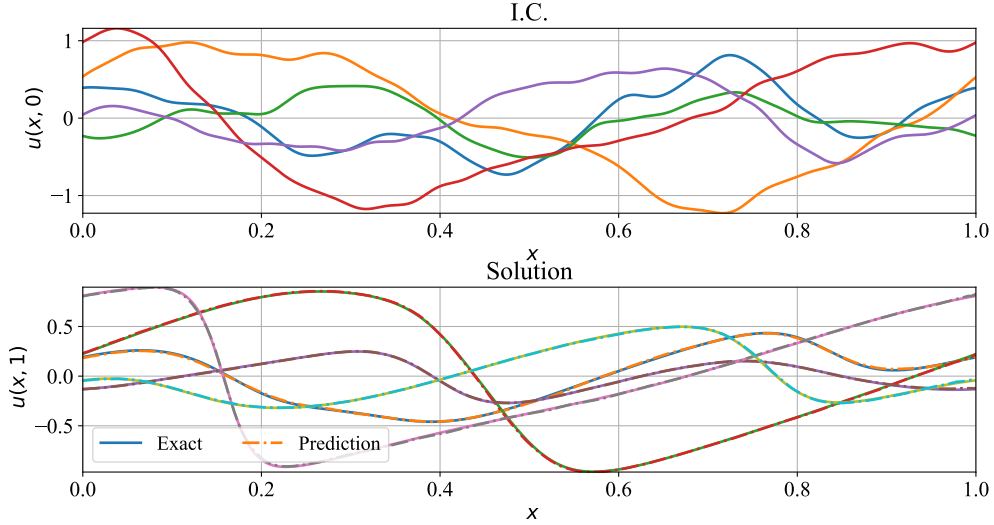


Figure 5 1D Burgers equation with periodic boundary conditions at 1024 spatial resolution. (top) Initial condition at $t = 0$, where different colored lines represent different initial value conditions. (bottom) Color-matched solid/dashed lines represent true/predicted solutions for each initial condition of 1D Burgers equation at $t = 1$.

1D time-dependent Burgers equation with discontinuity in the solution field: For small values of the viscosity parameter ν , the Burgers equation causes a sharp jump in the solution field. Modeling such sharp jumps in the solution field is extremely challenging. In this example, our objective is to understand how the operator’s initial conditions lead to a sharp jump in the solution field. The 1D Burgers equation, in the following form, can be employed to simulate sharp jumps in the solution field:

$$\begin{aligned}
 \partial_t u(x, t) + u(x, t) \partial_x u(x, t) &= \frac{0.01}{\pi} \partial_{xx} u(x, t), \quad x \in [-1, 1], t \in [0, 1] \\
 u(x = -1, t) &= u(x = 1, t) = 0, \quad x \in [-1, 1], t \in [0, 1] \\
 u(x, 0) &= -\sin(\pi x) + \zeta \sin(\pi x), \quad x \in [-1, 1].
 \end{aligned}
 \tag{4.3}$$

Where $\zeta \in [0, 0.5]$ is a random number. The aim is to learn the operator mapping the solution fields at the time steps $t \in [0, 10]$ to the solution fields up to time steps $t \in (10, 50]$ defined by $\mathcal{D} : u|_{(-1,1) \times [0,10]} \mapsto u|_{(-1,1) \times [10,50]}$. Data with a time step of $\Delta t = 0.02$ and a spatial resolution of 512 were used for training and testing. The dataset taken from Ref. [28].

Results: The true, predicted, and error results for an initial condition are shown in the first three subplots of Figure 6. From Figure 6 and Table 3, we can conclude that the prediction results obtained using U-WNO are accurate. The third subplot shows that the error is relatively large after $t = 0.4$ s (the white line in the figure), while the four plots in the last row depict the true and predicted solutions at $t = 0.4$ s, $t = 0.54$ s, $t = 0.76$ s and $t = 0.98$ s. Visually, there is no difference between the predicted and true

solutions. These show that the proposed U-WNO can accurately solve the 1D Burgers equation with sharp jump cases within the solution field.

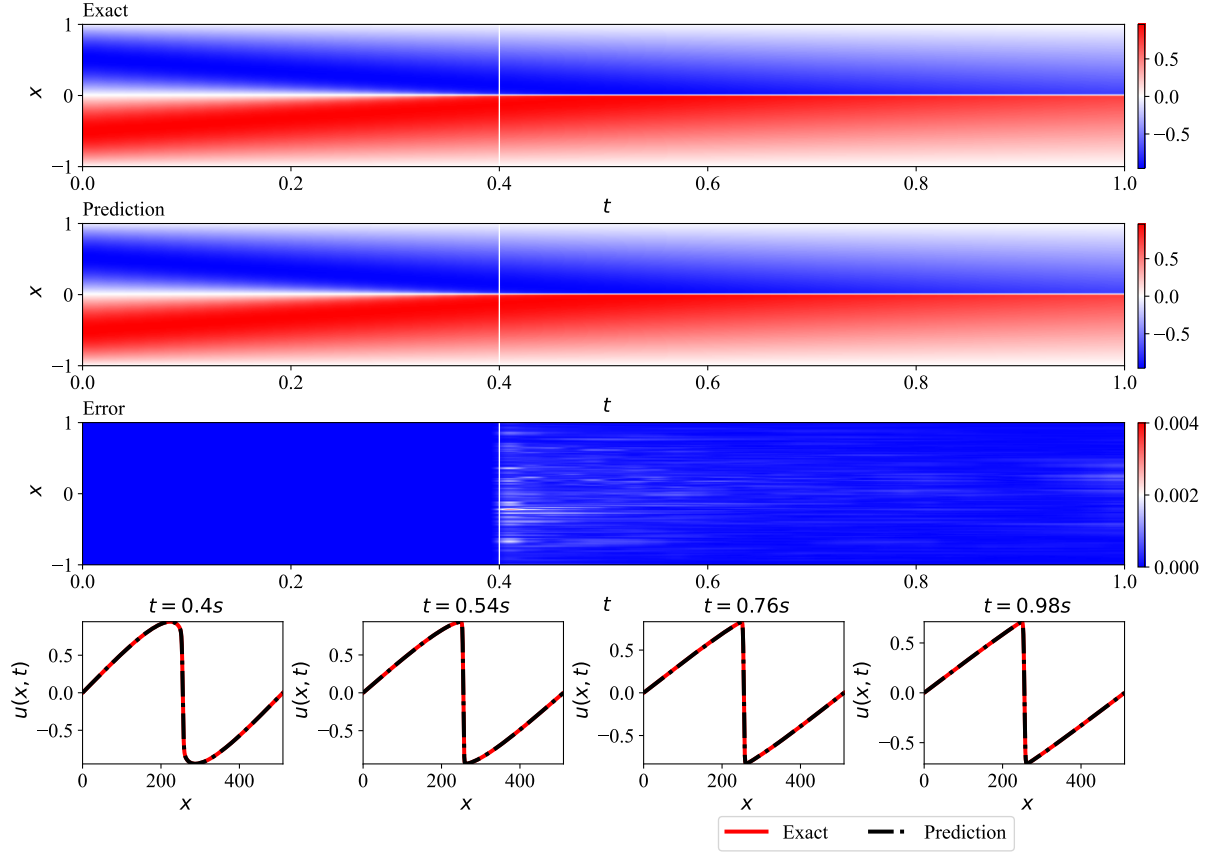


Figure 6 1D Burgers equation with a discontinuity in the solution field. The first three subplots illustrate the truth solutions, prediction ones, and errors, respectively. The four subplots in the last row depict the predicted and true solutions for the four moments with relatively large errors.

4.2. 1D wave advection equation

The wave advection equation describes the solution to a scalar in a given velocity field. The wave advection equation with periodic boundary conditions has the following form:

$$\begin{aligned} \partial_t u(x, t) + \nu \partial_x u(x, t) &= 0, \quad x \in (0, 1), t \in (0, 1) \\ u(x - \pi, t) &= u(x + \pi, t), \quad x \in (0, 1), t \in (0, 1). \end{aligned} \quad (4.4)$$

Here $\nu \in \mathbb{R}^{+*}$ denotes the velocity of the stream. The initial condition is,

$$u(x, 0) = h1_{\{c-\frac{\omega}{2}, c+\frac{\omega}{2}\}} + \sqrt{\max(h^2 - (a(x-c))^2, 0)}. \quad (4.5)$$

Here, the value of $\{c, \omega, h\}$ is randomly chosen as $[0.3, 0.7] \times [0.3, 0.6] \times [1, 2]$. For $\nu = 1$, the solution of the advection equation is $u(x, t) = u_0(x - t)$, the time step is 0.025, and the spatial discrete points are 40, resulting in a resolution of 40×40 advection equation solution. The dataset is taken from Ref. [40]. We first learn the mapping from the initial condition $u(x, 0)$ to the solution at $t = 1$:

$$\text{Case I: } \mathcal{G}_1 : u(x, 0) \mapsto u(x, t = 1),$$

Then learn the operator mapping from the initial condition $u(x, 0)$ to the solution of the whole domain

$$\text{Case II: } \mathcal{G}_2 : u(x, 0) \mapsto u(x, t).$$

Results: For case I, The prediction results and mean test L_2 relative error are shown in Figure 7 and Table 3. From Table 3, we can conclude that U-WNO significantly reduces the error compared to WNO. Figure 7 shows that there is almost no difference between the predicted and true results. This shows that U-WNO solves this problem well.

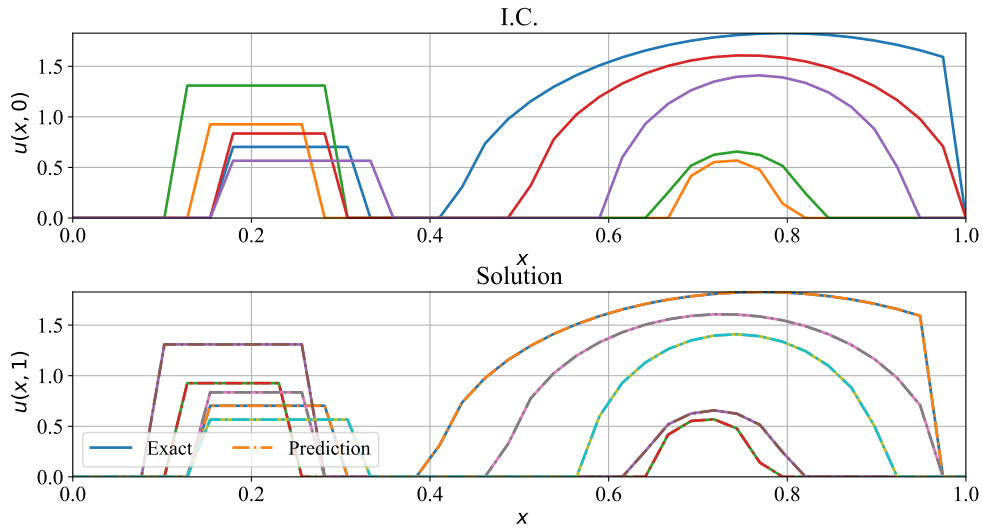


Figure 7 1D wave advection equation with periodic boundary conditions at 40×40 spatial resolution. (top) Initial condition at $t = 0$. (bottom) True and predicted solutions of 1D wave advection equation at $t = 1$.

For case II: The prediction results and mean L_2 relative errors are shown in Figure 8 and Table 3. Except for FNO and MWT which have slightly higher errors, DeepONet, dgFNO+, WNO, and U-WNO all have errors less than 1%, while the proposed U-WNO achieves the lowest error with an error less than 0.1%.

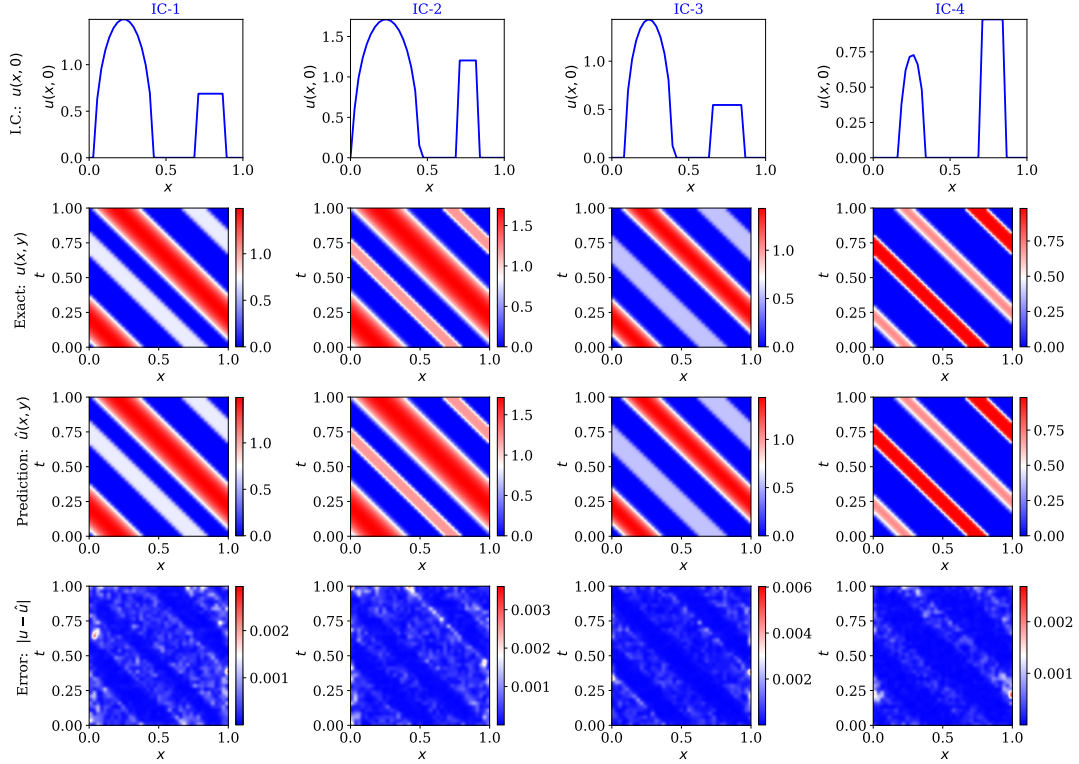


Figure 8 Wave advection equation with periodic boundary conditions with a resolution of 40×40 . The figure shows the true solution, the predicted solution, and the error corresponding to the initial conditions in Eq.(4.5)

4.3. 2D darcy flow equation

The 2D Darcy flow equation is widely used for fluid modeling. In this subsection, we consider Darcy flows of the following form

$$\begin{aligned}
 -\nabla \cdot (a(x, y) \nabla u(x, y)) &= f(x, y), \quad x, y \in (0, \mathbb{R}) \\
 u(x, y) &= u_0(x, y), \quad x, y \in \partial(0, \mathbb{R}).
 \end{aligned}
 \tag{4.6}$$

Where $a(x, y)$ represents the coefficients, the Darcy flow is defined in a rectangular field: $x \times y \in (0, 1)^2$. In this example, we select the initial condition $u_0(x, y) = 0$ and the source function $f(x, y) = 1$. The aim is to learn the operator $D : a(x, y) \mapsto u(x, y)$. The coefficients $a(x, y)$ are generated according to $a \sim \psi_{\#} \mathcal{N}(0, (-\Delta + 9I)^{-2})$ with zero Neumann boundary conditions on the Laplacian. The map $\psi : \mathbb{R} \rightarrow \mathbb{R}$ takes the value 12 in the positive part of the real line and 3 in the negative part, defined pointwise in the forward direction. The dataset is taken from Ref. [24]. During training, the spatial resolution is 85×85 .

Results: The prediction results of the 2D Darcy flow in the rectangular domain are shown in Figure 9, and the mean test L_2 relative error are shown in the Table 3. In this case, it can be observed that the error of U-WNO is the lowest. In Figure 9, it can be concluded that the difference between the true and

predicted solutions is small.

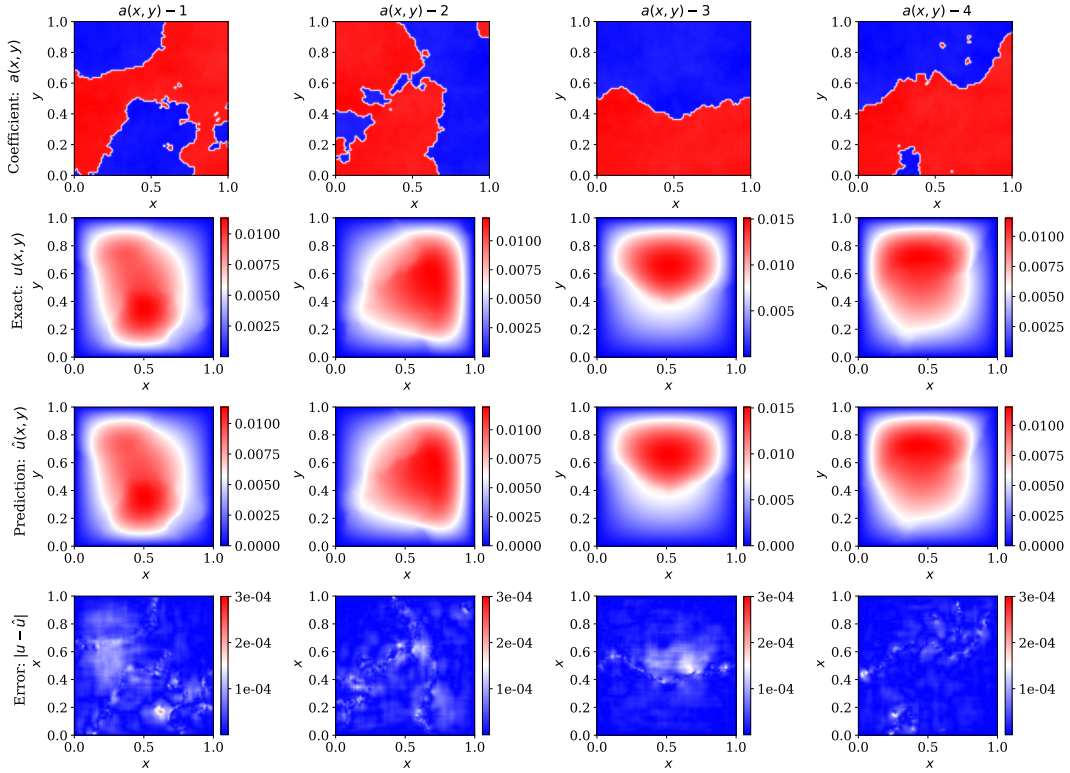


Figure 9 Darcy flow in a rectangular domain with spatial resolution 85×85 . For different coefficients, the solution field is obtained using the proposed U-WNO. The figure shows the predicted solutions, true solutions, and errors.

2D Darcy flow equation with a notch in triangular domain: Here, we consider the Darcy flow equation with a notch in triangular domain with coefficients $a(x, y) = 0.1$ and source function $f(x, y) = -1$. The aim is to learn the operator that maps the boundary conditions to the solution field, defined as $\mathcal{D} : u(x, y)|_{\partial\omega} \mapsto u(x, y)$. The dataset is taken from Ref. [40].

Results: The prediction solutions and mean test L_2 relative error are shown in Figure 10 and Table 3. From the values in Table 3, the error of U-WNO is the lowest, and the error is less than 1/3 of the WNO. The error between the true value and the prediction can also be observed in Figure 10, and it can be further noted that the predicted solution yields accurate predictions both in the smooth region and near the notch, which indicates that the proposed U-WNO can learn nonlinear operators under complex geometric conditions with higher accuracy than WNO.

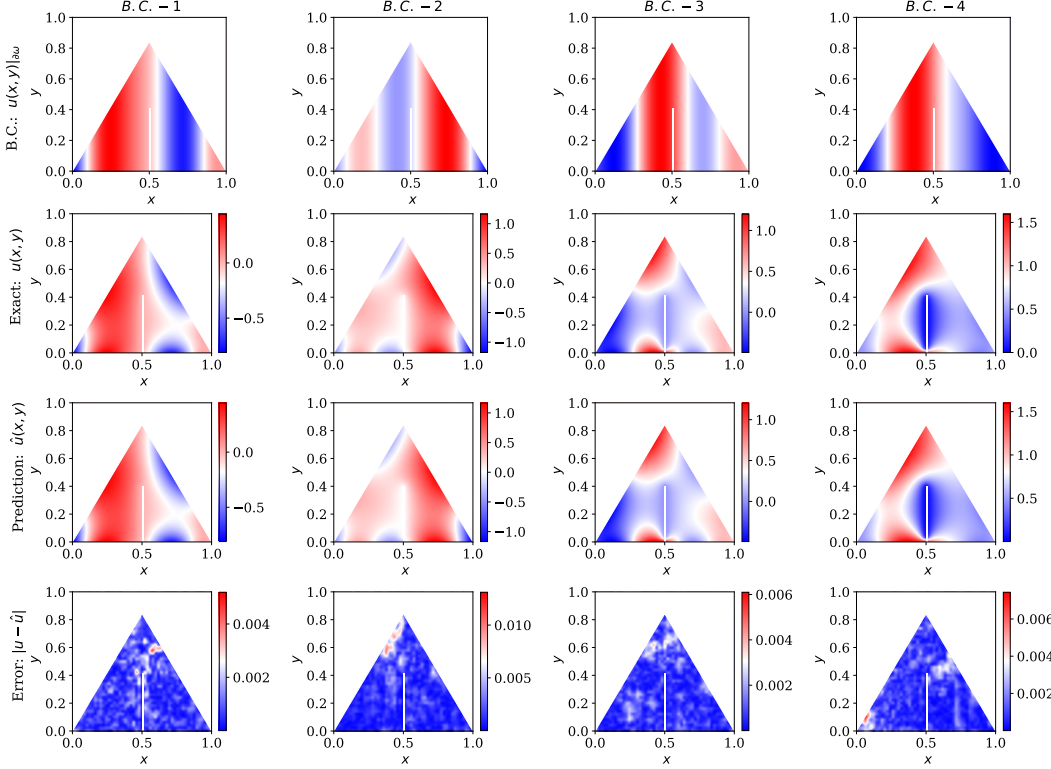


Figure 10 Darcy flow in a triangular domain with a spatial resolution of 51×51 . By using the proposed U-WNO model, the predicted solutions, true solutions, and errors are obtained under different boundary conditions.

4.4. 2D Allen-Cahn equation

The Allen-Cahn equation is commonly used for predicting chemical reactions and phase separation in multicomponent alloys. The 2D Allen-Cahn equation is as follows.

$$\begin{aligned}
 \partial_t u(x, y, t) &= \epsilon \Delta u(x, y, t) + u(x, y, t) - u(x, y, t)^3, & x, y \in (0, 3), t \in [0, 10] \\
 u(x = 0, y, t) &= u(x = 3, y, t), & y \in (0, 3), t \in [0, 10] \\
 u(x, y = 0, t) &= u(x, y = 3, t), & x \in (0, 3), t \in [0, 10] \\
 u(x, y, 0) &= u_0(x, y), & x, y \in (0, 3)
 \end{aligned} \tag{4.7}$$

Where $\epsilon \in \mathbb{R}^+$ is responsible for the amount of diffusion. The problem is defined on a periodic boundary of $\epsilon = 10^{-3}$, and the initial conditions are generated from a Gaussian random field with the following kernel:

$$\mathcal{K}(x, y) = \tau^{(\alpha-1)} (\pi^2(x^2 + y^2) + \tau^2)^{\frac{\alpha}{2}}, \tag{4.8}$$

where $\tau = 15$ and $\alpha = 1$. The aim here is to learn the operator $\mathcal{D} : u_0(x, y) \mapsto u(x, y, 10)$. Training and testing were performed on a resolution of 43×43 . The dataset is taken from Ref. [28].

Results: The mean test L_2 relative error and prediction results of the proposed U-WNO for different initial conditions are shown in Table 3 and Figure 11. The values in Table3 show that U-WNO obtains the

lowest prediction error, which is less than 1/2 of the error obtained by WNO and slightly less than 0.1%. In Figure 11, it can be concluded that the difference between the true and predicted results is small for all given initial conditions. This shows that the proposed U-WNO can accurately solve the nonlinear problem in 2D domain.

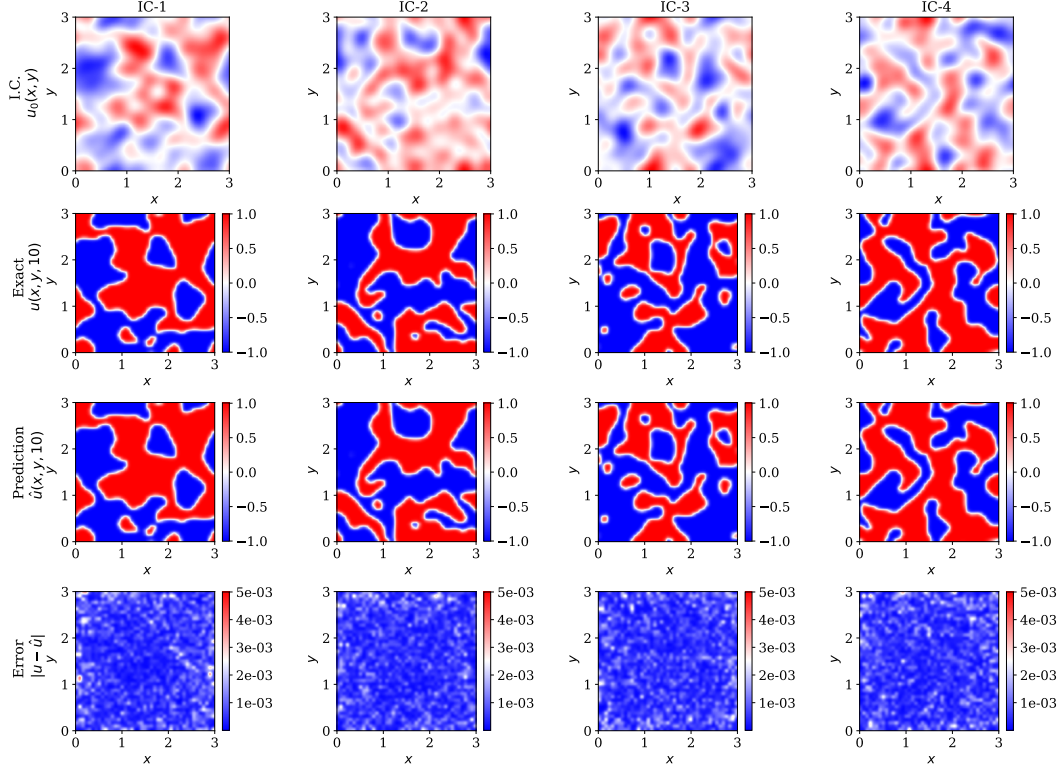


Figure 11 Allen-Cahn equation with periodic boundary conditions at resolution 43×43 . The predicted solutions, true solutions, and errors are obtained under different boundary conditions by using the proposed U-WNO model.

4.5. Non-homogeneous Poisson equation

The Poisson equation with a source term $f(x, y)$ and periodic boundary condition is expressed as:

$$\begin{aligned} \partial_{xx}u + \partial_{yy}u &= f(x, y), \quad x \in [-1, 1], \quad y \in [-1, 1] \\ u(x = -1, y) &= u(x = 1, y) = u(x, y = -1) = u(x, y = 1) = 0. \end{aligned} \quad (4.9)$$

In this example, the aim is to learn that the mapping between the source function $f(x, y)$ and the solution $u(x, y)$ is defined as $D : f(x, y) \mapsto u(x, y)$. Source function we choose $f(x, y) = 16\beta\pi^2(\cos(4\pi y)\sin(4\pi x) + \sin(4\pi x)(\cos(4\pi y) - 1)) - \alpha\pi^2(\cos(\pi y)\sin(\pi x) + \sin(\pi x)(\cos(\pi y) + 1))$. Then the solution is $u(x, y) = \alpha \sin(\pi x)(1 + \cos(\pi y)) + \beta \sin(2\pi x)(1 - \cos(2\pi y))$. $\alpha, \beta \in [-2, 2]$ are uniformly distributed random numbers. The samples of the training and testing instances are yielded by varying the variable α and β . A resolution of 85×85 was used for training and testing.

Results: The results in Figure 11 include the source function, the true solution, the predicted solution, and the prediction error. The results clearly show that the predicted and true solutions obtained by the proposed U-WNO are in good agreement. In addition, from the results shown in Table 3, the mean L_2 relative test error of U-WNO is lower than the error of WNO and FNO, reaching 0.044%, which indicates that U-WNO can learn nonlinear operators from source functions to solutions in 2D domain.

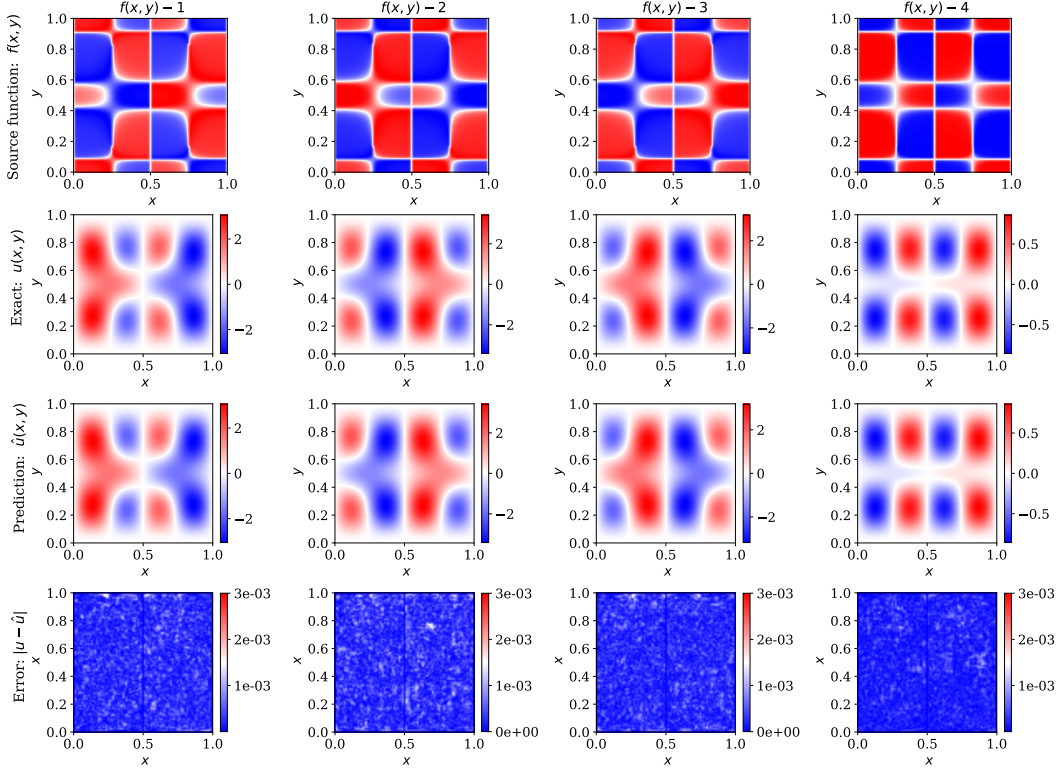


Figure 12 The proposed U-WNO maps the source function $f(x, y)$ of the Non-homogeneous Poisson equation to the corresponding solution $u(x, y)$ with a spatial resolution of 85×85 , the corresponding real solution, prediction, and error composition of the result.

4.6. 2D Navier–Stokes equation

Navier-Stokes equation is often used in air flows around aircraft wings, ocean currents, thermodynamics, etc. The 2D incompressible Navier-Stokes equations in the vorticity velocity form are of the following form.

$$\begin{aligned}
 \partial_t \omega(x, y, t) + u(x, y, t) \cdot \nabla \omega(x, y, t) &= \nu \Delta \omega(x, y, t) + f(x, y), & x, y \in (0, 1), t \in (0, T] \\
 \nabla \cdot u(x, y, t) &= 0, & x, y \in (0, 1), t \in [0, T] \\
 \omega(x, y, 0) &= \omega_0(x, y), & x, y \in (0, 1)
 \end{aligned} \tag{4.10}$$

where $\nu \in \mathbb{R}$, $f(x, y)$ is the fluid viscosity and the source function. $u(x, y, t)$ and $\omega(x, y, t)$ are the velocity and vorticity fields of the fluid, and the viscosity is taken as $\nu = 10^{-3}$. The aim is to learn the operator

mapping time step $t \in [0, 10]$ of vorticity field to the time step $t \in (10, 20]$ of the vorticity field, defined as $D : \omega|_{(0,1)^2 \times [0,10]} \mapsto \omega|_{(0,1)^2 \times [10,20]}$. The initial vorticity $\omega_0(x, y)$ by Gaussian random field simulation for the $\omega_0(x, y) = \mathcal{N}(0, 7^{3/2}(-\Delta + 49I)^{-2.5})$. The source function $f(x, y) = 0.1(\sin(2\pi(x+y)) + \cos(2\pi(x+y)))$. The dataset is taken from Ref. [28]. For training and testing, the spatial resolution is fixed to 64×64 .

Results: The prediction results for vorticity field at $t \in (10, 20]$ are given in Figure 13, along with the mean L_2 relative test error in Table 3. The results show that the prediction error of the proposed U-WNO is second only to MWT, lower than WNO and FNO, and less than 1/3 of the error of WNO. It can be speculated that the proposed U-WNO can learn the operators of the 2D time-dependent PDE with higher accuracy than WNO. Table 5 shows the long-term predictions of the Navier-Stokes equations by WNO and U-WNO. Although the training data only covers $t \in (0, 10]$, U-WNO still maintains a low error in the long-term prediction of $t \in (10, 40]$, indicating that it has some extrapolation ability.

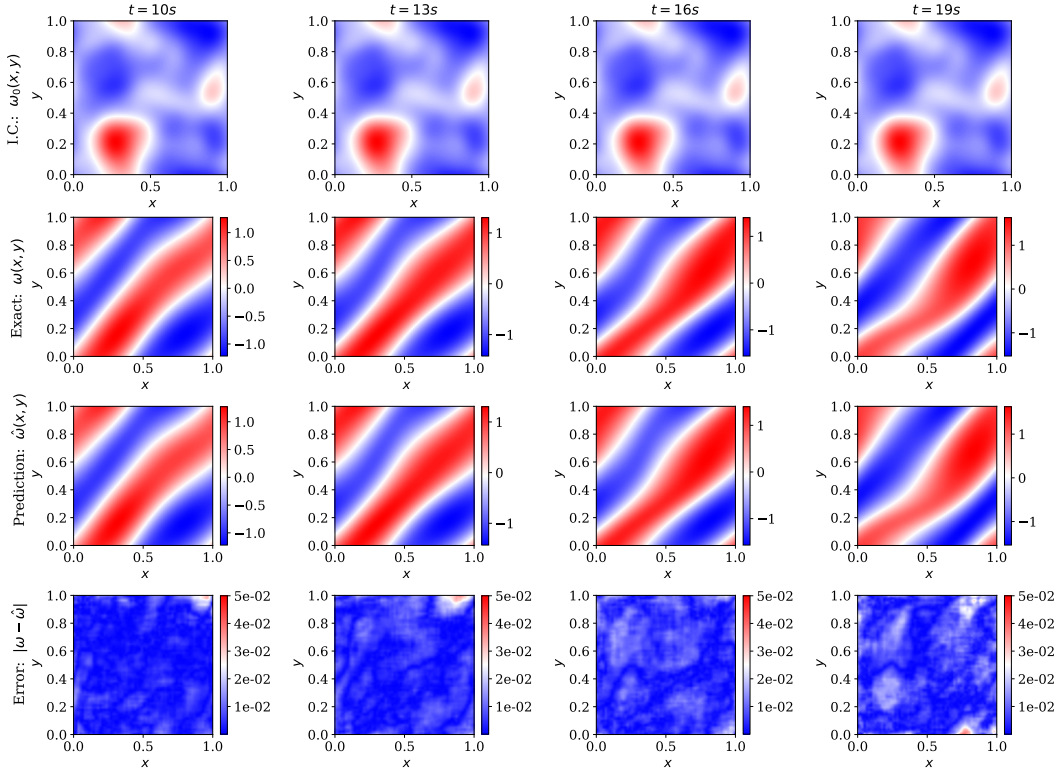


Figure 13 Navier-Stokes equations with a spatial resolution of 64×64 . Vorticity data at several initial time steps $t \in [0, 10]$ are used to predict vorticity data and error maps at subsequent time steps $t \in (11, 20]$.

Table 5 The mean L_2 relative error of the Navier-Stokes equations for long time predictions

Network architecture	$t \in (10, 20]$	$t \in (10, 25]$	$t \in (10, 30]$	$t \in (10, 35]$	$t \in (10, 40]$
U-WNO	0.96%	1.40%	2.77%	5.21%	8.06%
WNO	3.16%	4.34%	7.24%	11.60%	16.28%

5. Conclusions

In this paper, we propose the U-WNO neural operator, which integrates a U-Net path and an improved wavelet layer with an adaptive activation function. Unlike the baseline wavelet neural operator (WNO) that parameterizes only the integral kernel on coarse-grained discrete wavelet transform (DWT) scales, we introduce a U-Net pathway into the wavelet layer to enhance high-frequency feature extraction. By incorporating trainable slope parameters in the activation function, U-WNO mitigates spectral bias and further improves high-frequency representation capabilities. Additionally, we design residual connections inspired by neural network skip pathways to ensure spatial information completeness in each enhanced wavelet layer. Extensive numerical experiments compare U-WNO with WNO and other state-of-the-art operators (DeepONet, FNO, MWT). Results demonstrate that U-WNO achieves the lowest L_2 relative errors across multiple benchmarks and effectively learns nonlinear operators in complex geometries. Future work will focus on applying U-WNO to real-world engineering problems and developing a hybrid training framework that combines data-driven methods with physics-informed constraints.

Acknowledgements. *The authors are very much indebted to the referees for their constructive comments and valuable suggestions.*

Code Availability Statement

The code used to generate the findings of this study is openly available in GitHub at <https://doi.org/10.5281/zenodo.15612292>.

References

- [1] Matiur Rahman Minar and Jibon Naher. Recent advances in deep learning: An overview. *arXiv preprint arXiv:1807.08169*, 2018.
- [2] Lokenath Debnath and Lokenath Debnath. *Nonlinear partial differential equations for scientists and engineers*. Springer, 2005.
- [3] Lawrence C Evans. *Partial differential equations*, volume 19. American Mathematical Society, 2022.
- [4] Douglas Samuel Jones, Michael Plank, and Brian D Sleeman. *Differential equations and mathematical biology*. Chapman and Hall/CRC, 2009.
- [5] Charles A Taylor, Thomas JR Hughes, and Christopher K Zarins. Finite element modeling of blood flow in arteries. *Computer methods in applied mechanics and engineering*, 158(1-2):155–196, 1998.
- [6] J Austin Cottrell, Thomas JR Hughes, and Yuri Bazilevs. *Isogeometric analysis: toward integration of CAD and FEA*. John Wiley & Sons, 2009.

- [7] Yang Zhang. A finite difference method for fractional partial differential equation. *Applied Mathematics and Computation*, 215(2):524–529, 2009.
- [8] Robert Eymard, Thierry Gallouët, and Raphaèle Herbin. Finite volume methods. *Handbook of numerical analysis*, 7:713–1018, 2000.
- [9] Shagan Sah. Machine learning: A review of learning types. *Preprints*, 2020.
- [10] Pejman Tahmasebi, Serveh Kamrava, Tao Bai, and Muhammad Sahimi. Machine learning in geo-and environmental sciences: From small to large scale. *Advances in Water Resources*, 142:103619, 2020.
- [11] Maziar Raissi, Paris Perdikaris, and George E Karniadakis. Physics-informed neural networks: A deep learning framework for solving forward and inverse problems involving nonlinear partial differential equations. *Journal of Computational physics*, 378:686–707, 2019.
- [12] Justin Sirignano and Konstantinos Spiliopoulos. Dgm: A deep learning algorithm for solving partial differential equations. *Journal of computational physics*, 375:1339–1364, 2018.
- [13] Bing Yu et al. The deep ritz method: a deep learning-based numerical algorithm for solving variational problems. *Communications in Mathematics and Statistics*, 6(1):1–12, 2018.
- [14] Joaquin Vanschoren. Meta-learning: A survey. *arXiv preprint arXiv:1810.03548*, 2018.
- [15] Chuanqi Tan, Fuchun Sun, Tao Kong, Wenchang Zhang, Chao Yang, and Chunfang Liu. A survey on deep transfer learning. In *Artificial Neural Networks and Machine Learning–ICANN 2018: 27th International Conference on Artificial Neural Networks, Rhodes, Greece, October 4–7, 2018, Proceedings, Part III 27*, pages 270–279. Springer, 2018.
- [16] Somdatta Goswami, Cosmin Anitescu, Souvik Chakraborty, and Timon Rabczuk. Transfer learning enhanced physics informed neural network for phase-field modeling of fracture. *Theoretical and Applied Fracture Mechanics*, 106:102447, 2020.
- [17] Linlin Zhong, Bingyu Wu, and Yifan Wang. Accelerating physics-informed neural network based 1d arc simulation by meta learning. *Journal of Physics D: Applied Physics*, 56(7):074006, 2023.
- [18] Alex Nichol and John Schulman. Reptile: a scalable metalearning algorithm. *arXiv preprint arXiv:1803.02999*, 2(3):4, 2018.
- [19] Xu Liu, Xiaoya Zhang, Wei Peng, Weien Zhou, and Wen Yao. A novel meta-learning initialization method for physics-informed neural networks. *Neural Computing and Applications*, 34(17):14511–14534, 2022.
- [20] Yuyan Chen, Bin Dong, and Jinchao Xu. Meta-mgnet: Meta multigrid networks for solving parameterized partial differential equations. *Journal of computational physics*, 455:110996, 2022.
- [21] Zhaojun Bai, Patrick M Dewilde, and Roland W Freund. Reduced-order modeling. *Handbook of numerical analysis*, 13:825–895, 2005.
- [22] Yanlai Chen and Shawn Koohy. Gpt-pinn: Generative pre-trained physics-informed neural networks toward non-intrusive meta-learning of parametric pdes. *Finite Elements in Analysis and Design*, 228:104047, 2024.
- [23] Lu Lu, Pengzhan Jin, and George Em Karniadakis. Deeponet: Learning nonlinear operators for identifying differential equations based on the universal approximation theorem of operators. *arXiv preprint arXiv:1910.03193*, 2019.
- [24] Zongyi Li, Nikola Kovachki, Kamyar Azizzadenesheli, Burigede Liu, Kaushik Bhattacharya, Andrew Stuart, and Anima Anandkumar. Fourier neural operator for parametric partial differential equations. *arXiv preprint arXiv:2010.08895*, 2020.
- [25] Zongyi Li, Nikola Kovachki, Kamyar Azizzadenesheli, Burigede Liu, Kaushik Bhattacharya, Andrew Stuart, and Anima Anandkumar. Neural operator: Graph kernel network for partial differential equations. *arXiv preprint arXiv:2003.03485*, 2020.
- [26] Zongyi Li, Nikola Kovachki, Kamyar Azizzadenesheli, Burigede Liu, Andrew Stuart, Kaushik Bhattacharya, and Anima Anandkumar. Multipole graph neural operator for parametric partial differential equations. *Advances in Neural*

- Information Processing Systems*, 33:6755–6766, 2020.
- [27] Ronald N Bracewell. The fourier transform. *Scientific American*, 260(6):86–95, 1989.
- [28] Tapas Tripura and Souvik Chakraborty. Wavelet neural operator for solving parametric partial differential equations in computational mechanics problems. *Computer Methods in Applied Mechanics and Engineering*, 404:115783, 2023.
- [29] Tapas Tripura and Souvik Chakraborty. Wavelet neural operator: a neural operator for parametric partial differential equations. *arXiv preprint arXiv:2205.02191*, 2022.
- [30] Dequan Zhang, Xu Han, Chao Jiang, Jie Liu, and Qing Li. Time-dependent reliability analysis through response surface method. *Journal of Mechanical Design*, 139(4):041404, 2017.
- [31] Olaf Ronneberger, Philipp Fischer, and Thomas Brox. U-net: Convolutional networks for biomedical image segmentation. In *Medical image computing and computer-assisted intervention—MICCAI 2015: 18th international conference, Munich, Germany, October 5-9, 2015, proceedings, part III 18*, pages 234–241. Springer, 2015.
- [32] Nasim Rahaman, Aristide Baratin, Devansh Arpit, Felix Draxler, Min Lin, Fred Hamprecht, Yoshua Bengio, and Aaron Courville. On the spectral bias of neural networks. In *International conference on machine learning*, pages 5301–5310. PMLR, 2019.
- [33] Ameya D Jagtap, Kenji Kawaguchi, and George Em Karniadakis. Adaptive activation functions accelerate convergence in deep and physics-informed neural networks. *Journal of Computational Physics*, 404:109136, 2020.
- [34] Ameya D Jagtap, Yeonjong Shin, Kenji Kawaguchi, and George Em Karniadakis. Deep kronecker neural networks: A general framework for neural networks with adaptive activation functions. *Neurocomputing*, 468:165–180, 2022.
- [35] Ameya D Jagtap, Kenji Kawaguchi, and George Em Karniadakis. Locally adaptive activation functions with slope recovery for deep and physics-informed neural networks. *Proceedings of the Royal Society A*, 476(2239):20200334, 2020.
- [36] Arthur Jacot, Franck Gabriel, and Clément Hongler. Neural tangent kernel: Convergence and generalization in neural networks. *Advances in neural information processing systems*, 31, 2018.
- [37] Sifan Wang, Hanwen Wang, and Paris Perdikaris. On the eigenvector bias of fourier feature networks: From regression to solving multi-scale pdes with physics-informed neural networks. *Computer Methods in Applied Mechanics and Engineering*, 384:113938, 2021.
- [38] Gaurav Gupta, Xiongye Xiao, and Paul Bogdan. Multiwavelet-based operator learning for differential equations. *Advances in neural information processing systems*, 34:24048–24062, 2021.
- [39] Ingrid Daubechies. *Ten lectures on wavelets*. SIAM, 1992.
- [40] Lu Lu, Xuhui Meng, Shengze Cai, Zhiping Mao, Somdatta Goswami, Zhongqiang Zhang, and George Em Karniadakis. A comprehensive and fair comparison of two neural operators (with practical extensions) based on fair data. *Computer Methods in Applied Mechanics and Engineering*, 393:114778, 2022.